IEEE Access
Multidisciplinary ⋮ Rapid Review ⋮ Open Access Journal

Received 7 September 2023, accepted 16 September 2023, date of publication 20 September 2023,
date of current version 4 October 2023.

Digital Object Identifier 10.1109/ACCESS.2023.3317530

RESEARCH ARTICLE

Accurate, Efficient and Reliable Small-Signal Modeling Approaches for GaN HEMTs

SADDAM HUSAIN[1], ANWAR JARNDAL[2], (Senior Member, IEEE), MOHAMMAD HASHMI[1], (Senior Member, IEEE), AND FADHEL M. GHANNOUCHI[3], (Fellow, IEEE)

[1]Department of Electrical and Computer Engineering, School of Engineering and Digital Sciences, Nazarbayev University, 010000 Astana, Kazakhstan
[2]Department of Electrical Engineering, University of Sharjah, Sharjah, United Arab Emirates
[3]Department of Electrical and Computer Engineering, University of Calgary, Calgary, AB T2N 1N4, Canada

Corresponding author: Mohammad Hashmi (mohammad.hashmi@nu.edu.kz)

This work was supported by Nazarbayev University under Grant 021220CRP0222 and Grant 20122022FD4113.

ABSTRACT This article presents accurate, efficient and reliable small-signal model parameter extraction approaches applied to Gallium Nitride (GaN) High Electron Mobility Transistor (HEMT). Firstly, a scanning-based systematic model parameter extraction methodology is developed. Then, newly reported Optimization Algorithms (OAs) namely Marine Predators Algorithm (MPA), Pelican Optimization Algorithm (POA) and Tunicate Swarm Algorithm (TSA) in combination with direct extraction method are utilized to develop hybrid model parameter extraction methodologies. Lastly, both the scanning-based systematic and OA-based hybrid modelling procedures are thoroughly validated and demonstrated on a GaN HEMT grown on diamond substrate to identify their pros and cons in distinct application settings. Moreover, reliability, accuracy, convergence behavior, complexity and execution time of MPA-, POA- and TSA-based hybrid extraction procedures are also discussed. We found that both classes of the approaches are able to produce an excellent agreement between the measured and modelled S-parameters for a wide frequency range up to 40 GHz. However, OA-based hybrid modelling procedures are more physically relevant.

INDEX TERMS GaN HEMT, marine predators algorithm (MPA), parameter extraction, pelican optimization algorithm (POA), small-signal models (SSMs), tunicate swarm algorithm (TSA).

I. INTRODUCTION

Increased complexity and frequent innovations in latest wireless technologies have placed stringent requirements on the design of Radio Frequency Power Amplifiers (RFPAs) [1], [2]. Therefore, RFPAs should be meticulously designed to meet the evolving needs of innovative applications such as 5G, 6G, satellite communication, radar systems, Internet of Things (IoT) etc. [3], [4]. Gallium Nitride (GaN) High Electron Mobility Transistors (HEMTs) have been proven to be the most suitable transistors technologies for the design and innovation in RFPAs as these devices enable high output power with low currents allowing the small peripheral devices with low parasitic to operate at high frequencies with wide bandwidth capability [5]. However, accurate Small-Signal and Large-Signal Models (SSMs and LSMs) of GaN HEMT technology are extremely pertinent to realize this technology in the design of RFPAs and millimeter wave (mmWave) circuits [6], [7]. At this point, it is imperative to note that the SSMs are the foundational benchmark of the noise models, LSMs, and eventual design of low-noise amplifiers and RFPAs, therefore are considered essential [8], [9], [10], [11]. GaN-on-Diamond HEMT is a recently developed technology, which is getting popularity as this device manifests lower self-heating, thus renders better performance in contrast to its counterpart GaN-on-SiC HEMT [12]. Moreover, the higher thermal conductivity of diamond material with respect to SiC and Si (4 to 5 times) makes it an ideal alternative especially for the fabrication of high-power devices [12], [13].

Apparently, Small-Signal (SS) modelling approaches for GaN devices can be divided into three main categories: (a) physics-based modelling, which exploits the GaN

The associate editor coordinating the review of this manuscript and approving it for publication was Pedro Miguel Cabral.

HEMT's physical structure and equations those elucidate its operation [14], [15]; (b) behavioral modelling, that seeks to formulate a mathematical description between the GaN HEMT's response and the input perturbations [16], [17], [18], [19], [20], [21], [22] and (c) equivalent circuit-based modelling, which utilizes a lumped equivalent electronic circuit, whose parameters nearly depict GaN HEMT's physical operating mechanism and are extracted using the experimental data, thus regarded as an effective trade-off [23], [24], [25]. The main approaches to extract the SS Equivalent Circuit Model (ECM) parameters of GaN HEMT device can be bracketed in two categories. The first is known as direct extraction technique, which employs the conventional ''cold'' approach, is simple, straightforward and less-complex [26], [27], [28]. However, this approach does not cater for the distributed capacitive effects, thus its accuracy significantly diminishes at high operating frequency [28]. Furthermore, the direct extraction techniques are also highly sensitive to the measurement uncertainty [29]. The second approach amalgamates direct technique with Optimization Algorithm (OA)-driven extraction method, known as hybrid approach and are generally accurate but requires more time and effort to build and validate [29]. Nonetheless, an OA can render excellent results for one category of problems and fails for the other categories of problems as pointed by the no free lunch theorem. Therefore, recently, various OA-based hybrid extraction techniques have been reported to develop the SSMs of GaN HEMTs devices [29], [30], [31], [32], [33], [34].

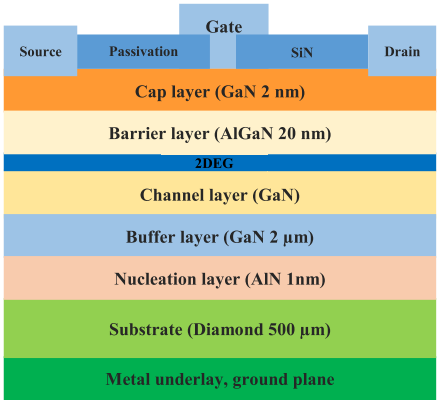

FIGURE 1. A general epitaxial structure of the DUT [35].

In this context, this paper explores and develops initially a scanning-based systematic and OA-based hybrid SS model parameter extraction methodologies. Recently reported Marine Predators Algorithm (MPA), Pelican Optimization Algorithm (POA) and Tunicate Swarm Algorithm (TSA) have been exploited to develop the hybrid approaches. Both the scanning-based systematic and OA-based hybrid approaches are applied on GaN-on-Diamond HEMT technology. Then, a thorough evaluation of the models developed using the scanning-based systematic and OA-based hybrid approaches is carried out in terms of reliability of the model parameters, physical relevance, execution time (the time required to complete the scanning process and running time of OAs for 50 iterations) and accuracy. Finally, a rigorous examination of OA-based hybrid approaches is also conducted using various metrics such as convergence of the solutions, complexity, execution time etc. Summing up, the major contributions of this paper with respect to others presented in literature are: (i) the demonstration of MPA-, POA- and TSA-based hybrid extraction methodologies for GaN-on-Dimaond HEMTs; (ii) a detailed examination of, at first, the scanning-based systematic and OA-based hybrid approaches, and at last, MPA-, POA- and TSA-based hybrid approaches in terms of simplicity of their implementations, accuracy, reliability, execution time and convergence behaviors and (iii) demonstration and evaluations of these techniques for the broad range of frequency (0.1 GHz to 40 GHz).

The next section spells out the details of the Device Under Test (DUT) and the ECM. Sections III and IV demonstrate the development and validation of the scanning-based systematic and OA-based hybrid model parameter extraction methodologies, respectively. The results and discussion are provided in Section V. Lastly, Section VI concludes the paper preceding with references.

II. DETAILS OF THE DEVICE UNDER TEST AND EQUIVALENT CIRCUIT MODEL

A. DETAILS OF THE DUT

A thorough discussion on physics and characterization of the DUT is published in [12], [13], and [35]. Briefly, Fig. 1 demonstrates the epitaxial structure of the considered DUT. The DUT is a GaN HEMT device grown on top of 500 µm diamond substrate. The fabrication of the device involves the growth of 1 nm AlN nucleation layer, 2 µm Fe-doped GaN based buffer layer, GaN based channel layer, barrier layer (20 nm AlGaN) and 2 nm GaN based Cap layer on top of the substrate. The barrier layer has been doped with 0.3 nm Al concentration (Al-mole). Furthermore, electron beam lithography has been used to realize the gate. The device has been fabricated with the specification of gate-drain spacing (L_{gd}), gate-source spacing (L_{gs}), gate finger width (W_g), gate number (N_g) and gate length (L) of 2 µm, 1 µm, 125 µm, 4 and 0.25 µm, respectively.

A N5245 Vector Network Analyzer (VNA) is employed for the RF characterization of the DUT and outputs are recorded in terms of real and imaginary S-parameters. Furthermore, the measurement setup also includes two bias tees, bias voltage source, RF wafer probe station, and a PC. Before taking the measurements, the VNA is calibrated using the line-reflect match technique with the help of calibration standard 104-783 from Cascade Microtech [13]. The device has been characterized with respect to gate to source voltage (V_{GS}), drain to source voltage (V_{DS}) and frequency (f), which incorporates a wide-range of 0.1 GHz to 40 GHz. Likewise, V_{GS} and V_{DS} incorporate wide-ranges, -3 V to 0 V and 0 V to 30 V, respectively.

B. SMALL-SIGNAL EQUIVALENT CIRCUIT MODEL

In this work, as depicted in Fig. 2, we are exploiting an identical SSECM reported in [35]. Conventionally, ECM is comprised of two disjointed parts: extrinsic part—contains bias-independent model elements and intrinsic part—which embodies bias-dependent model elements. In the adopted SSECM: C_{pga}, C_{pda}, C_{pgi} and C_{pdi} account for parasitic pad capacitances and inter-electrode or interconnections-engendered capacitances, respectively. Parasitic inductances and resistances induced from the metalization, distinct contacts etc. are expressed with L_g, L_s, L_d and R_g, R_s, R_d, respectively. Charging and discharging processes of the transistor are modelled with C_{gs}, C_{gd}, R_i and R_{gd}. Likewise, G_m, G_{ds} and τ characterize trans-, output-conductances and transit time, respectively.

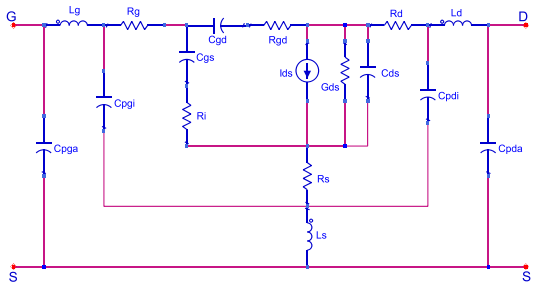

FIGURE 2. Small-signal equivalent circuit model adopted in this work.

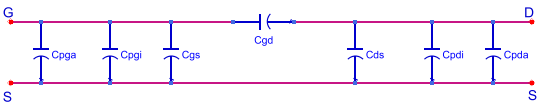

FIGURE 3. Topology representing the low-frequency equivalent circuit ($\leq$ 1 GHz) of Cold-FET operation.

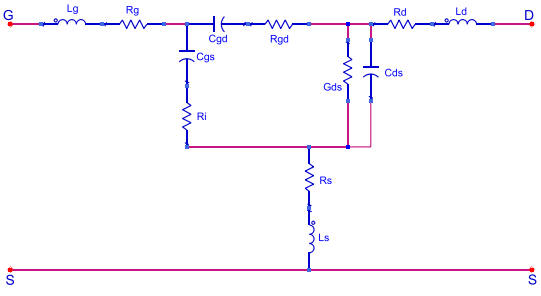

FIGURE 4. Topology representing ECM following deembedding of capacitors under unbiased state.

III. THE SCANNING-BASED SYSTEMATIC MODEL PARAMETER EXTRACTION METHODOLOGY

This work makes use of the similar scanning-based systematic modelling methodology reported in [35]. Fig. 6 elucidates the methodology that has been implemented here to

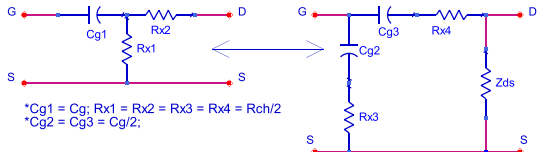

FIGURE 5. T and π based equivalent circuits for the intrinsic part under unbiased state for high frequency operation.

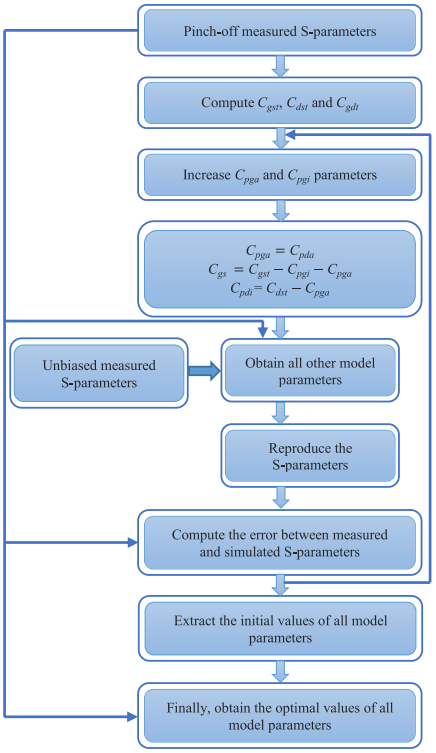

FIGURE 6. The utilized scanning-based systematic approach to extract the model parameters.

extract the SSECM's parameters that replicates the behavior at pinch-off. To achieve this, initially, total capacitances (C_{gst}, C_{gdt} and C_{dst}) are calculated at the Cold-FET pinch-off condition (V_{GS} = –3 V, V_{DS} = 0 V). At this juncture, the device has no channel current, therefore, SSECM topology under low-frequency operation ($\leq$ 1 GHz) can be represented by the simplified capacitive network as depicted in Fig. 3. For this network (see Fig. 3), Y-parameters can be written as follows:

$$\mathrm{Im}[Y_{11}] = j\omega(C_{pga} + C_{pgi} + C_{gs} + C_{gd}) \quad (1)$$

$$\mathrm{Im}[Y_{12}] = \mathrm{Im}[Y_{21}] = -j\omega C_{gd} \quad (2)$$

$$\mathrm{Im}[Y_{22}] = j\omega(C_{pda} + C_{pdi} + C_{ds} + C_{gd}). \quad (3)$$

From (1) to (3), total capacitances are extracted by simple linear regression analysis (see Fig. 7), where $C_{gst} = C_{pga} + C_{pgi} + C_{gs}$, $C_{gdt} = C_{gd}$ and $C_{dst} = C_{pda} + C_{pdi} + C_{ds}$. Once total capacitances are determined, a systematic search is carried out for C_{pga} and C_{pgi}. In this setting, C_{pga} and C_{pgi} are assigned incremental values within the

range of 0.01xC_{gst} and C_{gst} with the step size of 0.02xC_{gst} and scanned. For allocated values of C_{pga} and C_{pgi}, other capacitances are calculated (see (4) and (5)) with following assumptions: $C_{pga} = C_{pda}$, $C_{gdt} = C_{gd}$, and $C_{ds} = 0$ (which is typically the case under pinch-off).

$$C_{gs} = C_{gst} - C_{pga} - C_{pgi} \tag{4}$$
$$C_{pdi} = C_{dst} - C_{pga}. \tag{5}$$

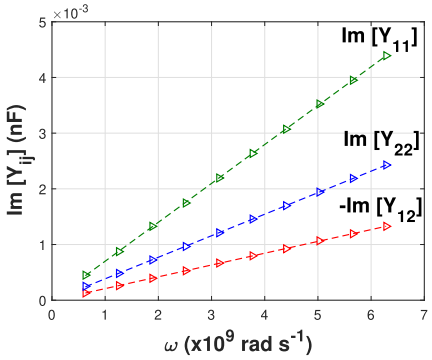

FIGURE 7. Simple linear regression analysis to extract total capacitances at the Cold-FET pinch-off condition.

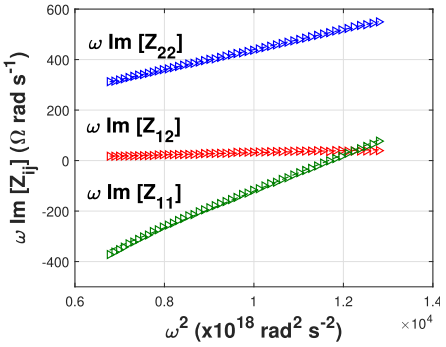

FIGURE 8. Extraction of parasitic inductances at the unbiased condition.

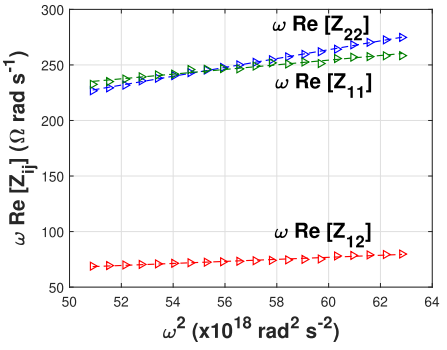

FIGURE 9. Extraction of parasitic resistances at the unbiased condition.

Then, unbiased measurement (V_{GS} = 0 V and V_{DS} = 0 V) is utilized to extract parasitic inductances and resistances. To realize this, firstly, C_{pga} and C_{pda} are deembedded and parasitic inductances are extracted. Thereafter, inductances, C_{pgi} and C_{pdi} values are deembedded and parasitic resistances are extracted. Under this scenario, due the absence of drain and gate currents, the effects of SSECM parameters namely G_m and τ can be ignored. SSECM topology following deembedding of capacitors under unbiased state is presented through Fig. 4. Moreover, at this point, it is well-known that the formed channel will be symmetrically depleted near the gate metallization. Therefore, we can assume $C_{gs} = C_{gd} = C_g$ and $R_i = R_{gd} = R_{ch}/2$ [35]. Also, the gate capacitance (C_g) avoids diode differential resistances [34] at high frequency, and simultaneously channel capacitance can be excluded [34]. Therefore, the intrinsic part of the transistor (see Fig. 4) can be expressed as π-network and its corresponding T-network based equivalent circuits (see Fig. 5) under unbiased state for high frequency operation [35]. Consequently, we can write the Z-parameters at the unbiased state using the T-network representation of the intrinsic part by (6) to (8).

$$Z_{11} = (R_g + R_s + R_{ch}/2) + j\omega(L_g + L_s) + 1/j\omega(C_g) \tag{6}$$
$$Z_{12} = Z_{21} = R_s + R_{ch}/2 + j\omega L_s \tag{7}$$
$$Z_{22} = (R_d + R_s + R_{ch}) + j\omega(L_d + L_s). \tag{8}$$

At this instance, the parasitic inductances and resistances can be extracted from the slope of ωIm [Z_{ij}] verses ω^2 (this approach accounts the effects of C_{pgi} and C_{pdi} during the extraction of parasitic inductances) and ωRe [Z_{ij}] verses ω^2, respectively (see Figs. 8 and 9). Here, Im [Z_{ij}] and Re [Z_{ij}] are basically imaginary and real parts derived from (6) to (8), respectively. Once the extrinsic elements' values (parasitic capacitances, inductances and resistances) are known, intrinsic elements are computed based on standard formulas [34] using intrinsic Y-parameters following the deembedding of extrinsic elements. S-parameters are then simulated using the extracted model parameters and error between measured and predicted S-parameters is computed as follows:

$$\varepsilon_{ab} = \frac{|\mathrm{Re}(\delta S_{ab,m})| + |\mathrm{Im}(\delta S_{ab,m})|}{W_{ab}} \tag{9}$$

where, a, b = 1, 2, m = 1, 2, . . . , N and W_{ab} is defined as follows:

$$W_{ab} = \max[|S_{ab}|], \quad a, b = 1, 2;\ a \neq b \tag{10}$$
$$W_{ab} = 1 + |S_{ab}|, \quad a = 1, 2. \tag{11}$$

Here, N and δS represent number of data samples and the deviation between the measured and predicted S-parameters, respectively. W_{ab}, weighting factor, de-emphasizes data corresponding to higher reflection coefficients owing to the involved higher measurement uncertainty [35]. The above-mentioned extraction procedure is repeated for each scanned value of C_{pga} and C_{pgi} and corresponding model parameters and error values are stored in a matrix (see the flow-chart given in Fig. 6). The obtained results are sorted with respect to error and the combination of C_{pga} and C_{pgi}, which gives

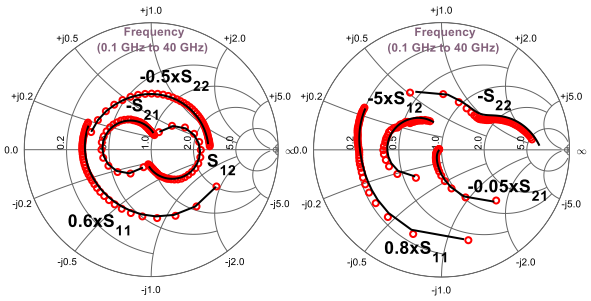

FIGURE 10. Simulated (lines) and measured (symbols) S-parameters at (left) V_{GS} = –3 V and V_{DS} = 0 V; (right) V_{GS} = –1 V and V_{DS} = 10 V (using the scanning-based systematic model parameter extraction methodology).

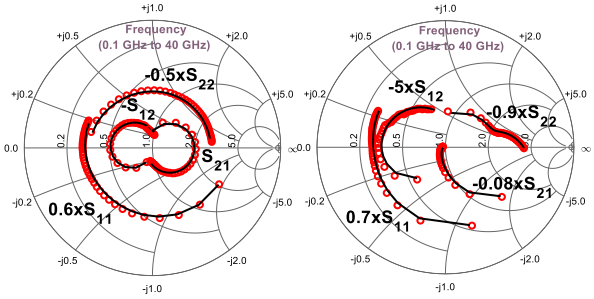

FIGURE 11. Simulated (lines) and measured (symbols) S-parameters at (left) V_{GS} = –2.5 V and V_{DS} = 2.5 V; (right) V_{GS} = 0 V and V_{DS} = 5 V (using the scanning-based systematic model parameter extraction methodology).

TABLE 1. Obtained values of the SSECM parameters using the scanning-based systematic model parameter extraction methodology.

Model Elements	V_{GS} = -3 V and V_{DS} = 0 V	V_{GS} = -1 V and V_{DS} = 10 V	V_{GS} = -2.5 V and V_{DS} = 2.5 V
C_{pga} (fF)	4.8667	4.8667	4.8667
C_{pda} (fF)	4.8667	4.8667	4.8667
C_{pgi} (fF)	4.8667	4.8667	4.8667
C_{pdi} (fF)	169.8133	169.8133	169.8133
L_g (pH)	64.3886	64.3886	64.3886
L_s (pH)	0.68589	0.68589	0.68589
L_d (pH)	43.2408	43.2408	43.2408
$R_g(\Omega)$	1.3809	1.3809	1.3809
$R_s(\Omega)$	1.0515	1.0515	1.0515
$R_d(\Omega)$	3.5887	3.5887	3.5887
C_{gs} (fF)	486.9551	1053.5954	504.4434
C_{gd} (fF)	216.6123	127.2769	170.7636
C_{ds} (fF)	14.5464	84.1108	18.968
$R_i(\Omega)$	0.82854	1.0167	0.69902
$R_{gd}(\Omega)$	5.7852	19.6874	6.6395
G_m (mS)	0	251.8868	0.5849
G_{ds} (mS)	0	6.7428	0.24065
τ (ps)	0	1.1238	8.7885
Error	0.0633	0.16686	0.0962

the minimum error is selected. The validity of the modelling scheme is verified at Cold-FET pinch-off condition, (V_{GS} = –1 V, V_{DS} = 10 V) and (V_{GS} = –2.5 V, V_{DS} = 2.5 V). The obtained values of model elements at these biasing conditions are given in Table 1. Measured and predicted S-parameters are also plotted at Cold-FET pinch-off condition, (V_{GS} = –1 V, V_{DS} = 10 V), (V_{GS} = –2.5 V, V_{DS} = 2.5 V) and (V_{GS} = 0 V, V_{DS} = 5 V) as depicted through Figs. 10 and 11. We can observe from results that the developed approach accurately simulates the measured characteristics for extensive 0.1 GHz to 40 GHz frequency operation including device physics related issues such as kink effect, RF-dc dispersion effect, memory effect etc. in GaN device [36], [37]. Furthermore, Figs. 12 and 13 demonstrate the intrinsic elements' behaviors with respect to frequency at (V_{GS} = –1 V, V_{DS} = 10 V) and (V_{GS} = 0 V, V_{DS} = 5 V). We can notice, almost constant and frequency-independent behaviors of the intrinsic elements for the whole frequency range, which validate the accuracy of the model topology and the utilized scanning-based systematic modelling approach. Further discussion on the results are given in the Section V.

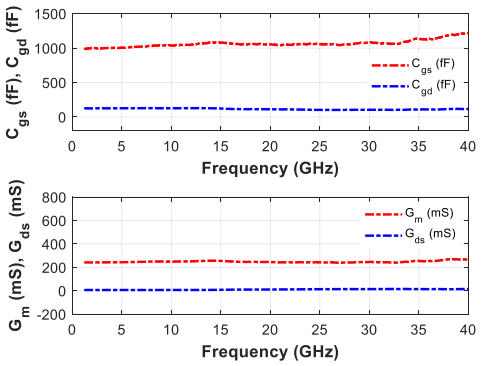

FIGURE 12. Behavior of intrinsic parameters with respect to frequency at V_{GS} = –1 V and V_{DS} = 10 V (using the scanning-based systematic model parameter extraction methodology).

IV. OPTIMIZATION ALGORITHMS-BASED HYBRID MODEL PARAMETER EXTRACTION METHODOLOGIES

This section reports reliable hybrid small-signal modelling of the same 4 × 125 μm GaN-on-Diamond HEMT based on MPA, POA and TSA optimization techniques.

A. MARINE PREDATORS ALGORITHM

MPA is a nature-inspired metaheuristic OA, which is mainly motivated by predominant Lévy and Brownian foraging movements in ocean predators and the precise engagement rate policy found in biological interactions of predator and prey. It acts according to rules that naturally govern these movements in marine ecosystems. MPA employs Lévy flight and Brownian motion in different application scenarios in order to develop an efficient explorer-exploiter framework. Based on the varying velocity ratio and emulation of the entire life of predator and prey, the MPA optimization process can be divided into three chief categories: (1) high velocity ratio; (2) almost equal velocity ratio and (3) low velocity ratio, which represent the states when predator is moving slower

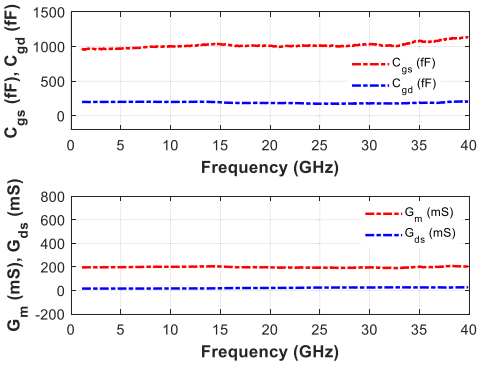

FIGURE 13. Behavior of intrinsic parameters with respect to frequency at V_{GS} = 0 V and V_{DS} = 5 V (using the scanning-based systematic model parameter extraction methodology).

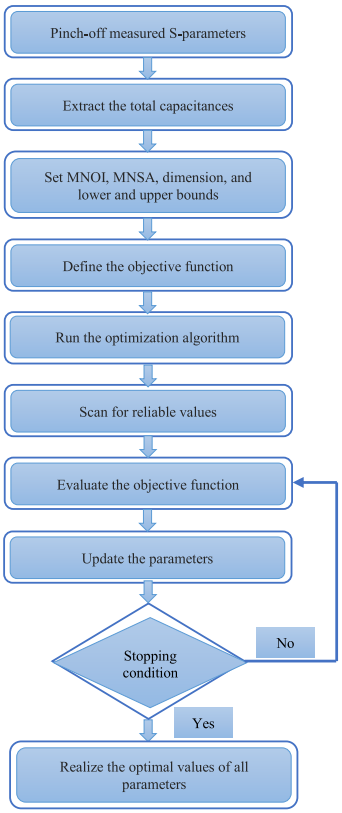

FIGURE 14. General extraction procedure employed with MPA, POA and TSA optimization algorithms.

than prey, same as prey and faster than prey, respectively. Phase 1, high velocity ratio (v $\geq$ 10), represents exploration of the MPA, where the algorithm simulates the predator's stillness. The mathematical model that simulates this phase is given in (12).

$$\text{While Iter} < \frac{1}{3}\text{MNOI}$$
$$\overrightarrow{\text{stepsize}_i} = \vec{R}_B \otimes \left(\overrightarrow{\text{Elite}_i} - \vec{R}_B \otimes \overrightarrow{\text{Prey}_i}\right)$$
$$\overrightarrow{\text{Prey}_i} = \overrightarrow{\text{Prey}_i} + \text{P}.\vec{R} \otimes \overrightarrow{\text{stepsize}_i}. \quad (12)$$

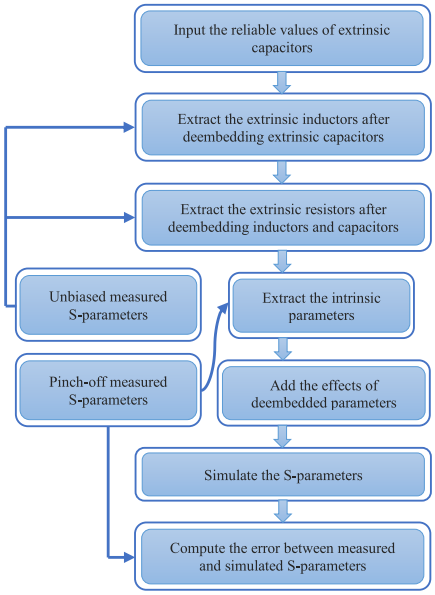

FIGURE 15. Defined objective function and evaluation exploited by MPA, POA and TSA optimization algorithms.

Here, i = 1, 2, . . . , n. MNOI, $\overrightarrow{\text{Elite}_i}$, P, R, R_B, $\otimes$ and $R_B \otimes \overrightarrow{\text{Prey}_i}$ denote maximum number of iteration, values corresponding to the *Elite* matrix, constant number equals to 0.5, uniform random numbers between 0 to 1, Brownian motion's normal distribution, element-wise multiplications and movement of the prey, respectively. The mathematical models that simulates the phase 2, almost equal velocity ratio (v $\approx$ 1), is given in (13). In this phase, prey moves in Lévy (responsible for exploitation) and predator moves in Brownian (responsible for exploration). The first half of the populations responsible for exploitation, are represented by (13).

$$\text{While } \frac{1}{3}\text{MNOI} < \text{Iter} < \frac{2}{3}\text{MNOI}$$
$$\overrightarrow{\text{stepsize}_i} = \vec{R}_L \otimes \left(\overrightarrow{\text{Elite}_i} - \vec{R}_L \otimes \overrightarrow{\text{Prey}_i}\right)$$
$$\overrightarrow{\text{Prey}_i} = \overrightarrow{\text{Prey}_i} + \text{P}.\vec{R} \otimes \overrightarrow{\text{stepsize}_i}. \quad (13)$$

In (13), R_L and $R_L \otimes \overrightarrow{\text{Prey}_i}$ denote Lévy movement and prey's movement in Lévy manner. Likewise, the second half of the populations responsible for exploration are represented by (14), where, CF and $R_B \otimes \overrightarrow{\text{Elite}_i}$ represent a parameter to regulate the step size and predator's movement in Brownian fashion, respectively.

$$\overrightarrow{\text{stepsize}_i} = \vec{R}_B \otimes \left(\vec{R}_B \otimes \overrightarrow{\text{Elite}_i} - \overrightarrow{\text{Prey}_i}\right)$$
$$\overrightarrow{\text{Prey}_i} = \overrightarrow{\text{Elite}_i} + \text{P.CF} \otimes \overrightarrow{\text{stepsize}_i}. \quad (14)$$

In the last phase, phase 3, low velocity ratio (v = 0.1) exhibits exploitation ability of MPA, where predator is moving in

Lévy manner as depicted in (15).

$$\begin{aligned} &\text{While Iter} > \frac{2}{3}\text{MNOI} \\ &\overrightarrow{\text{stepsize}_i} = \overrightarrow{R}_L \otimes \left(\overrightarrow{R}_L \otimes \overrightarrow{\text{Elite}_i} - \overrightarrow{\text{Prey}_i}\right) \\ &\overrightarrow{\text{Prey}_i} = \overrightarrow{\text{Elite}_i} + \text{P.CF} \otimes \overrightarrow{\text{stepsize}_i}. \end{aligned} \tag{15}$$

Stagnation in local minimums is a major problem with optimization techniques. MPA avoids this by simulating the eddy formation and Fish Aggregating Devices (FADs) effects. The mathematical representation of the same is given in (16), where case 1 and case 2 are simulated if r $\leq$ FADs and if r $>$ FADs, respectively. The comprehensive details on MPA is reported in [38].

$$\overrightarrow{\text{Prey}_i} = \begin{cases} \overrightarrow{\text{Prey}_i} + \text{CF}\left[\overrightarrow{X}_{\min} + \overrightarrow{R} \otimes (\overrightarrow{X}_{\max} - \overrightarrow{X}_{\min})\right] \cdot \otimes \overrightarrow{U} \\ \overrightarrow{\text{Prey}_i} + [\text{FADs}(1-\text{r}) + \text{r}]\left(\overrightarrow{\text{Prey}_{r1}} - \overrightarrow{\text{Prey}_{r2}}\right) \end{cases} \tag{16}$$

As stated earlier, we exploited MPA to extract the SSECM parameters for the same GaN-on-Diamond HEMT. The general extraction procedure employed with OAs (MPA, POA and TSA) to extract the parameters those best fit the measurement behavior is shown in Fig. 14, whilst the optimization function utilized by OAs is given in Fig. 15. The following points summarize the each step taken to develop and validate the MPA-based hybrid model parameter extraction methodology:

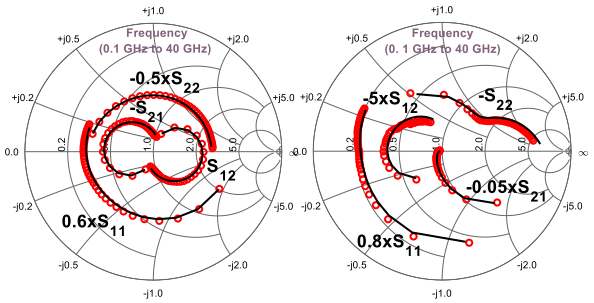

FIGURE 16. Simulated (lines) and measured (symbols) S-parameters at (left) V_{GS} = –3 V and V_{DS} = 0 V; (right) V_{GS} = –1 V and V_{DS} = 10 V (using the MPA-based hybrid approach).

Step 1: firstly, C_{gst}, C_{gdt} and C_{dst} are extracted at the Cold-FET pinch-off condition using direct extraction technique (see Section III) and lower and upper boundaries are defined for the optimization variables C_{pga}, C_{pgi}, C_{pda} and C_{pdi}.

Step 2: MNOI, maximum number of search agents (MNSA) and dimension are defined. It is imperative to mention that these parameters are iteratively tuned for the best performance. We found that MNOI as 50 and MNSA as 2500 render the optimal performance. Then, the initial search agents (prey) populations are initialized. To avoid any non-reliable value, we employed reliability conditions given in (17).

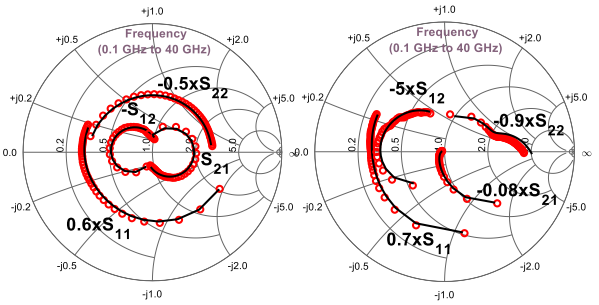

FIGURE 17. Simulated (lines) and measured (symbols) S-parameters at (left) V_{GS} = –2.5 V and V_{DS} = 2.5 V; (right) V_{GS} = 0 V and V_{DS} = 5 V (using the MPA-based hybrid approach).

TABLE 2. Obtained values of the SSECM parameters using the MPA-based hybrid model parameter extraction methodology.

Model Elements	V_{GS} = -3 V and V_{DS} = 0 V	V_{GS} = -1 V and V_{DS} = 10 V	V_{GS} = -2.5 V and V_{DS} = 2.5 V
C_{pga} (fF)	6.0814	6.0814	6.0814
C_{pda} (fF)	1.9095	1.9095	1.9095
C_{pgi} (fF)	4.8667	4.8667	4.8667
C_{pdi} (fF)	174.68	174.68	174.68
L_g (pH)	64.3591	64.3591	64.3591
L_s (pH)	0.6749	0.6749	0.6749
L_d (pH)	43.3738	43.3738	43.3738
$R_g(\Omega)$	1.3805	1.3805	1.3805
$R_s(\Omega)$	1.0529	1.0529	1.0529
$R_d(\Omega)$	3.5997	3.5997	3.5997
C_{gs} (fF)	487.3104	1053.3712	503.944
C_{gd} (fF)	216.8384	127.2015	170.6785
C_{ds} (fF)	12.4565	69.8314	17.125
$R_i(\Omega)$	0.77246	0.95841	0.65264
$R_{gd}(\Omega)$	5.7265	18.723	6.5408
G_m (mS)	0	251.8639	0.58467
G_{ds} (mS)	0	6.7446	0.25343
τ (ps)	0	1.1432	8.265
Error	0.060343	0.1605	0.07693

$$\begin{aligned} C_{pga} + C_{pgi} &< C_{gst} \\ C_{pda} + C_{pdi} &< C_{dst} \end{aligned} \tag{17}$$

Step 3: parasitic inductances and resistances are extracted using the unbiased measurement (see Section III).

Step 4: all the extrinsic model elements are deembedded from the pinch-off S-parameters to extract the intrinsic elements (see Section III).

Step 5: using both extracted extrinsic and intrinsic model elements, S-parameters are simulated after reversing the deembedding process. Then, the error between the modelled and measured S-parameters are calculated using the same error function (see Section III) as given in (9-11). According to the fittest solution, MPA sets up the Elite matrix.

Step 6: now, MPA updates its parameters based on the Iteration Number (Iter). When the current Iter is less than

one-third of MNOI (Iter $<$ $\frac{1}{3}$MNOI), the prey is updated based on the mathematical formula in (12). When the Iter is between one-third and two-third of MNOI ($\frac{1}{3}$MNOI $<$ Iter $<$ $\frac{2}{3}$MNOI), then the first half of the population (prey) is updated based on (13) and the other half is updated based on (14). But if the Iter is greater than two-third of MNOI (Iter $>$ $\frac{2}{3}$MNOI), prey population is updated based on (15). Thereafter, after completing the memory saving process it updates the Elite matrix and apply FADs effects using (16).

Step 7: then, the entire process is repeated until the termination condition is met (MNOI = 50).

Step 8: lastly, the MPA-based hybrid extraction methodology is validated for the same test conditions as above-mentioned (Cold-FET pinch-off condition, (V_{GS} = –1 V, V_{DS} = 10 V) and (V_{GS} = –2.5 V, V_{DS} = 2.5 V). The obtained values of SSECM's elements corresponding to the minimum error between modelled and measured S-parameters are given in Table 2. Furthermore, simulation plots at the same above conditions namely Cold-FET pinch-off condition, (V_{GS} = –1 V, V_{DS} = 10 V), (V_{GS} = –2.5 V, V_{DS} = 2.5 V) and (V_{GS} = 0 V, V_{DS} = 5 V) are shown in Figs. 16 and 17. In addition, the behaviors of intrinsic elements with respect to frequency at (V_{GS} = –1 V, V_{DS} = 10 V) and (V_{GS} = 0 V, V_{DS} = 5 V) are also plotted (see Figs. 18 and 19). It is imperative from the results that the SSECM developed using MPA-based hybrid approach is able to accurately mimic the measurement data behavior including the device physics related issues such as kink effect, RF-dc dispersion effect, memory effect etc. [36], [37]. Reliability and accuracy of the developed model is further verified by near constant and frequency independent behaviors of the intrinsic elements for the entire frequency range. More discussion on the results will be provided in Section V.

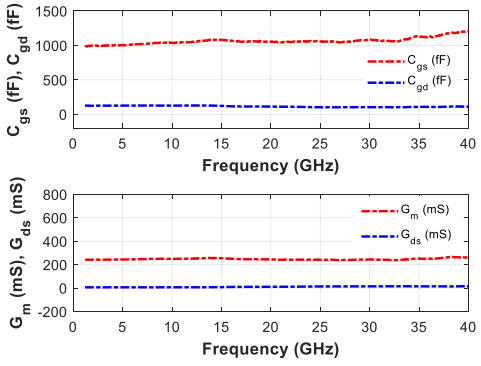

FIGURE 18. Behavior of intrinsic parameters with respect to frequency at V_{GS} = –1 V and V_{DS} = 10 V (using the MPA-based hybrid approach).

B. PELICAN OPTIMIZATION ALGORITHM

POA is a nature-inspired OA that simulates the hunting behavior of pelicans. Each pelican acts as a candidate solution in POA, population-based algorithm [39]. To update the candidate solutions, POA exploits the simulation of the hunting behavior in two stages:

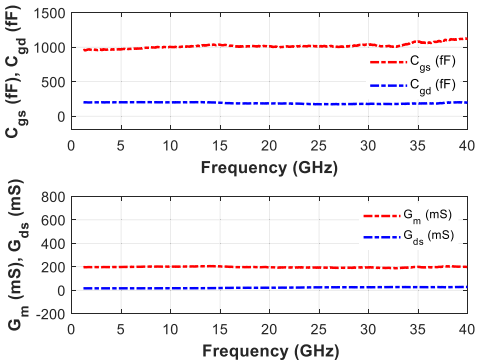

FIGURE 19. Behavior of intrinsic parameters with respect to frequency at V_{GS} = 0 V and V_{DS} = 5 V (using the MPA-based hybrid approach).

1) the movement of pelicans towards the prey (exploration phase)

2) pelicans' winging behavior on the water surface (exploitation phase)

In POA, the first phase is simulated as (18), where $x_{i,j}^{P1}$, I (responsible for exploration), p_j and F_p represent updated position of ith pelican in the jth dimension, random number as either 1 or 2, prey's location in jth dimension and value of objective function, respectively.

$$x_{i,j}^{P1} = \begin{cases} x_{i,j} + \text{rand}.(p_j - I.x_{i,j}), F_p < F_i. \\ x_{i,j} + \text{rand}.(x_{i,j} - p_j), \text{else} \end{cases} \tag{18}$$

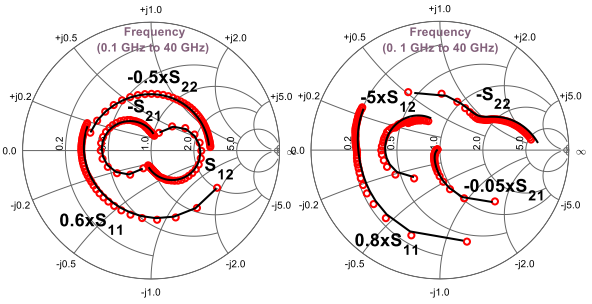

FIGURE 20. Simulated (lines) and measured (symbols) S-parameters at (left) V_{GS} = –3 V and V_{DS} = 0 V; (right) V_{GS} = –1 V and V_{DS} = 10 V (using the POA-based hybrid approach).

The second phase, which enables the POA to have better exploitation ability is mathematically represented as (19), where $x_{i,j}^{P2}$, R, R.$(1-\frac{t}{MNOI})$—mainly responsible for exploitation, and t denote updated position of ith pelican in the jth dimension, constant number (R = 2), nearby area around $x_{i,j}$ and current iteration, respectively. POA updates the positions of each member according to stages 1 and 2 and repeats this process until the termination condition is met.

$$x_{i,j}^{P2} = x_{i,j} + R.\left(1 - \frac{t}{MNOI}\right).(2.\text{rand} - 1).x_{i,j}. \tag{19}$$

As stated earlier, POA is used to develop the SSECM for the same GaN-on-Diamond HEMT device. The steps taken to

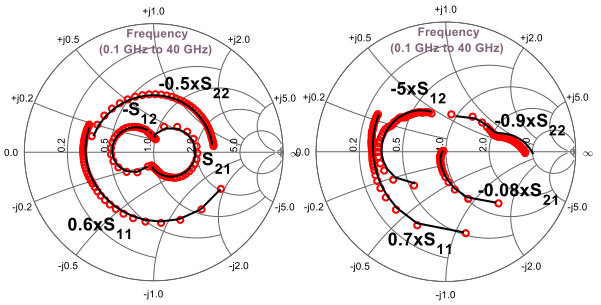

FIGURE 21. Simulated (lines) and measured (symbols) S-parameters at (left) V_{GS} = –2.5 V and V_{DS} = 2.5 V; (right) V_{GS} = 0 V and V_{DS} = 5 V (using the POA-based hybrid approach).

develop and validate the POA-based hybrid model parameter extraction methodology are given below:

Step 1: we followed the same step 1 of MPA.

Step 2: using the same procedure of MPA, we set MNOI and MNSA equals to 50 and 2500, respectively. Then, we initialized the initial position of pelicans and used the same reliability conditions (see (17)) to filter out the non-reliable values.

Step 3: Parasitic inductances, resistances, intrinsic elements, and objective function are calculated according to the same steps (see MPA's steps 3, 4 and 5).

Step 4: to get to the next iteration, as explained earlier, positions of pelicans are updated using two-stage formation—pelicans' movement towards prey and winging behavior according to (18)-(19).

Step 5: Similar to MPA, POA stops when the termination condition is met (MNOI = 50).

Step 6: at last, POA-based hybrid extraction procedure is validated for the same test conditions as of MPA-based procedure. The results are demonstrated using the Table 3 and Figs. 20 and 21. We found that the POA-based hybrid extraction method provide exactly same results and intrinsic parameters' behaviors with respect to frequency as of MPA-based hybrid approach. Further details are given in Section V.

C. TUNICATE SWARM ALGORITHM

TSA is a metaheuristic OA, which simulates the tunicates' jet propulsion and swarm behaviors, through out the navigation and foraging process [40]. To employ the jet propulsion behavior, tunicates exploit three basic principles—1) conflict management between search agents; 2) their motion in the direction of best neighbour and 3) convergence in the direction of best search agent. These principles are mathematically modelled in TSA as follows: to evade the conflicts between the search agents, a variable $\vec{A}$, to account for new position of the search agent is proposed, where $\vec{A} = \vec{G}/\vec{M}$. $\vec{G}$, which is basically gravity, is defined as follows: $\vec{G} = c_2 + c_3 - \vec{F}$, where $\vec{F}$ signifies the horizontal movement of water flow in the ocean and represented as: $\vec{F} = 2.c_1$. c_1, c_2 and c_3 are randomly defined between 0 to 1 and

TABLE 3. Obtained values of the SSECM parameters using the POA-based hybrid model parameter extraction methodology.

Model Elements	V_{GS} = -3 V and V_{DS} = 0 V	V_{GS} = -1 V and V_{DS} = 10 V	V_{GS} = -2.5 V and V_{DS} = 2.5 V
C_{pga} (fF)	6.0814	6.0814	6.0814
C_{pda} (fF)	1.9095	1.9095	1.9095
C_{pgi} (fF)	4.8667	4.8667	4.8667
C_{pdi} (fF)	174.68	174.68	174.68
L_g (pH)	64.3591	64.3591	64.3591
L_s (pH)	0.6749	0.6749	0.6749
L_d (pH)	43.3738	43.3738	43.3738
$R_g(\Omega)$	1.3805	1.3805	1.3805
$R_s(\Omega)$	1.0529	1.0529	1.0529
$R_d(\Omega)$	3.5997	3.5997	3.5997
C_{gs} (fF)	487.3104	1053.3712	503.944
C_{gd} (fF)	216.8384	127.2015	170.6785
C_{ds} (fF)	12.4565	69.8314	17.125
$R_i(\Omega)$	0.77246	0.95841	0.65264
$R_{gd}(\Omega)$	5.7265	18.723	6.5408
G_m (mS)	0	251.8639	0.58467
G_{ds} (mS)	0	6.7446	0.25343
τ (ps)	0	1.1432	8.265
Error	0.060343	0.1605	0.07693

$\vec{M}$ imitates the social forces among the search agents and expressed as: $\vec{M} = [P_{min} + c_1.(P_{max} - P_{min})]$. Importantly, the variations in the parameters $\vec{A}$, $\vec{G}$ and $\vec{F}$ enable the TSA to have better exploration and exploitation. To model the second principle, the search agents while trying to shun the conflicts among them, move towards in the direction of best neighbor. Mathematically, it can be modelled as follows: $\vec{PD} = |\vec{FS} - \text{rand}.\overrightarrow{P_p(x)}|$, where $\vec{PD}$, x, $\vec{FS}$, $\overrightarrow{P_p(x)}$ and rand represent distance between tunicate and food source, current iteration, food source's current position, tunicate's current position and random number between [0, 1], respectively. The third principle is mathematically represented using (20).

$$\overrightarrow{P_p(x)} = \begin{cases} \vec{FS} + \vec{A}.\vec{PD}, & \text{if rand} \geq 0.5. \\ \vec{FS} - \vec{A}.\vec{PD}, & \text{if rand} < 0.5 \end{cases} \tag{20}$$

As explained earlier, TSA also incorporates the swarm behavior. To mathematically emulate this behavior, TSA utilizes first two optimal best solutions. TSA arranges the positions of other search agents using the first two optimal best solutions as given in (21).

$$\overrightarrow{P_p(x+1)} = \frac{\overrightarrow{P_p(x)} + \overrightarrow{P_p(x+1)}.}{2 + c_1} \tag{21}$$

Again, the following points summarize the each step taken to develop and validate the TSA-based hybrid model parameter extraction methodology:

Step 1: step 1 of TSA-based hybrid approach is same as of step 1 of MPA and POA.

Step 2: MNOI and MNSA are set to 50 and 2500, respectively. Then, the tunicates' population is initialized and and the same reliability conditions are employed (see (17)).

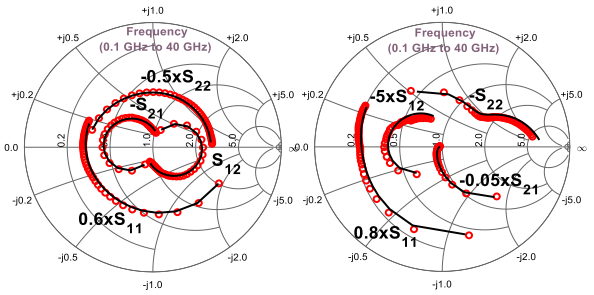

FIGURE 22. Simulated (lines) and measured (symbols) S-parameters at (left) V_{GS} = –3 V and V_{DS} = 0 V; (right) V_{GS} = –1 V and V_{DS} = 10 V (using the TSA-based hybrid approach).

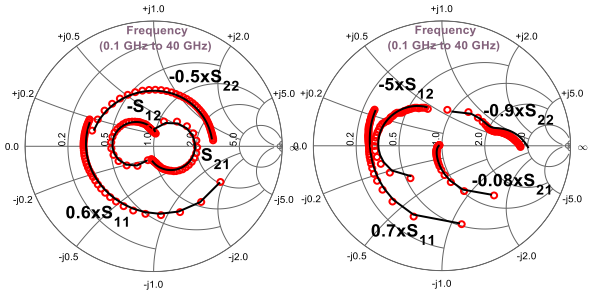

FIGURE 23. Simulated (lines) and measured (symbols) S-parameters at (left) V_{GS} = –2.5 V and V_{DS} = 2.5 V; (right) V_{GS} = 0 V and V_{DS} = 5 V (using the TSA-based hybrid approach).

TABLE 4. Obtained values of the SSECM parameters using the TSA-based hybrid model parameter extraction methodology.

Model Elements	V_{GS} = -3 V and V_{DS} = 0 V	V_{GS} = -1 V and V_{DS} = 10 V	V_{GS} = -2.5 V and V_{DS} = 2.5 V
C_{pga} (fF)	6.0815	6.0815	6.0815
C_{pda} (fF)	1.8849	1.8849	1.8849
C_{pgi} (fF)	4.8667	4.8667	4.8667
C_{pdi} (fF)	174.68	174.68	174.68
L_g (pH)	64.3592	64.3592	64.3592
L_s (pH)	0.67479	0.67479	0.67479
L_d (pH)	43.3749	43.3749	43.3749
$R_g(\Omega)$	1.3804	1.3804	1.3804
$R_s(\Omega)$	1.0529	1.0529	1.0529
$R_d(\Omega)$	3.5998	3.5998	3.5998
C_{gs} (fF)	487.3118	1053.3679	503.9449
C_{gd} (fF)	216.8364	127.2008	170.6772
C_{ds} (fF)	12.4945	69.7948	17.109
$R_i(\Omega)$	0.77246	0.95851	0.6528
$R_{gd}(\Omega)$	5.7269	18.724	6.5417
G_m (mS)	0	251.8615	0.58467
G_{ds} (mS)	0	6.7443	0.25323
τ (ps)	0	1.1435	8.2682
Error	0.060343	0.16046	0.076932

Step 3: using the same procedure of MPA and POA, parasitic inductances, parasitic resistances, intrinsic parameters and objective function are computed (see MPA's steps 3, 4 and 5), and the best search agent is identified.

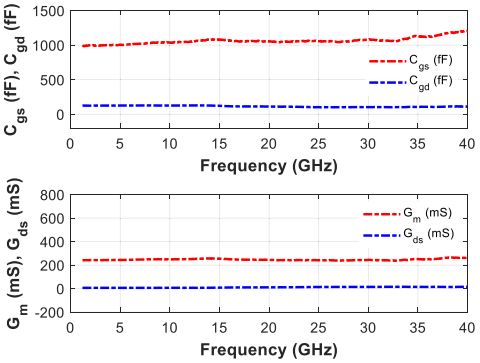

FIGURE 24. Behavior of intrinsic parameters with respect to frequency at V_{GS} = –1 V and V_{DS} = 10 V (using the TSA-based hybrid approach).

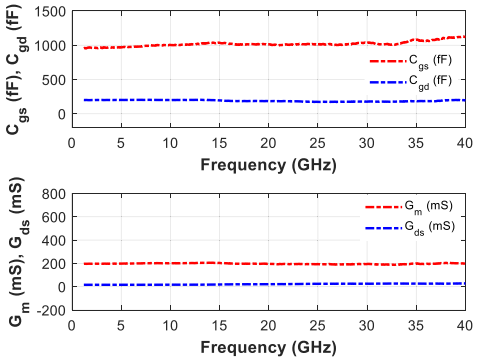

FIGURE 25. Behavior of intrinsic parameters with respect to frequency at V_{GS} = 0 V and V_{DS} = 5 V (using the TSA-based hybrid approach).

Step 4: search agents' positions are updated according to (21).

Step 5: again fitness value is calculated based on updated positions and if found to be better than the previous best, $\overrightarrow{P_p(x)}$ is updated.

Step 6: similar to others, the algorithm stops when MNOI becomes greater than 50 (termination criteria).

Step 7: the TSA-based hybrid approach is validated for the same test conditions as of MPA or POA. The results are depicted using Table 4 and Figs. 22 and 23. Furthermore, Figs. 24 and 25 demonstrate the intrinsic parameters' behaviors versus frequency. It can be clearly noticed from the results that the TSA-based hybrid extraction procedure is accurate, reliable and robust, and like MPA- and POA-based approaches mimics the measurement data behavior of the DUT including the device physics related issues such as kink effect, RF-dc dispersion effect, memory effect etc. [36], [37]. An in-depth discussion on the results are given in Section V.

V. RESULTS AND DISCUSSION

All the models presented in this paper are developed in MATLAB using the computer which specifications are as follows: Processor-Intel(R) Xeon(R) W-2135 CPU @3.70GHz; Installed RAM-128 GB; Windows Edition-Windows 10

TABLE 5. Evaluation of MPA-, POA- and TSA-based hybrid model parameter extraction methodologies.

Parameters	MPA	POA	TSA
Hyperparameters	MNOI and MNSA	MNOI and MNSA	MNOI and MNSA
Model's implementation	simple	simple	simple
Iterations	50	50	50
Error (%) (pinch-off)	6.0343	6.0343	6.0343
Execution time (s)	100.35	99.33	50.48

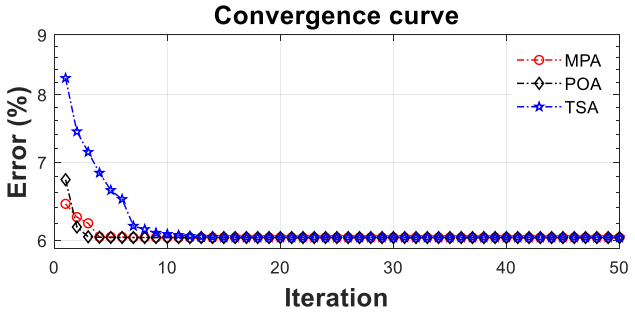

FIGURE 26. Convergence behavior of MPA, POA and TSA optimization algorithms.

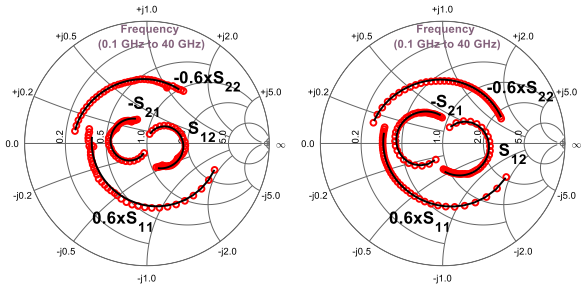

FIGURE 27. Simulated (lines) and measured (symbols) S-parameters at (left) V_{GS} = –4 V and V_{DS} = 0 V; (right) V_{GS} = –3 V and V_{DS} = 0 V (using the scanning-based systematic model parameter extraction methodology).

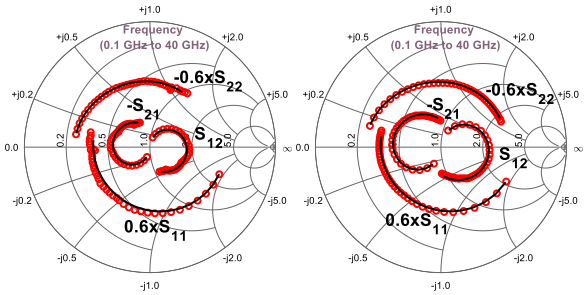

FIGURE 28. Simulated (lines) and measured (symbols) S-parameters at (left) V_{GS} = –4 V and V_{DS} = 0 V; (right) V_{GS} = –3 V and V_{DS} = 0 V (using the MPA-based hybrid approach).

Enterprise and Version-21H2. Initially, we developed a scanning-based systematic extraction procedure, and assumed C_{pga} = C_{pda}. This technique took 7.03 seconds

TABLE 6. Obtained values of the SSECM parameters using the scanning-based systematic model parameter extraction methodology.

Model Elements	GaN-on-Dia 2 x 100 μm	GaN-on-Dia 2 x 125 μm	GaN-on-Dia 4 x 125 μm
C_{pga} (fF)	2.1851	2.4889	4.8667
C_{pda} (fF)	2.1851	2.4889	4.8667
C_{pgi} (fF)	2.1851	2.4889	4.8667
C_{pdi} (fF)	74.7409	102.061	169.8133
L_g (pH)	60.0856	61.4606	64.3886
L_s (pH)	0.43142	0.4515	0.68589
L_d (pH)	39.1945	40.039	43.2408
$R_g(\Omega)$	2.4463	2.5863	1.3809
$R_s(\Omega)$	3.3534	1.9255	1.0515
$R_d(\Omega)$	9.7551	7.1212	3.5887
C_{gs} (fF)	201.3978	244.5995	486.9551
C_{gd} (fF)	62.1303	111.6456	216.6123
C_{ds} (fF)	12.2728	13.2469	14.5464
$R_i(\Omega)$	1.074	0.7593	0.82854
$R_{gd}(\Omega)$	14.2059	7.3835	5.7852
G_m (mS)	0	0	0
G_{ds} (mS)	0	0	0
τ (ps)	0	0	0
Error	0.0892	0.0588	0.0633

TABLE 7. Obtained values of the SSECM parameters using the MPA-based hybrid model parameter extraction methodology.

Model Elements	GaN-on-Dia 2 x 100 μm	GaN-on-Dia 2 x 125 μm	GaN-on-Dia 4 x 125 μm
C_{pga} (fF)	2.1851	3.2229	6.0814
C_{pda} (fF)	0.7692	1.8956	1.9095
C_{pgi} (fF)	2.0854	2.4889	4.8667
C_{pdi} (fF)	52.615	99.7152	174.68
L_g (pH)	60.1023	61.4607	64.3591
L_s (pH)	0.4323	0.4565	0.6749
L_d (pH)	39.2194	40.045	43.3738
$R_g(\Omega)$	2.4527	2.5873	1.3805
$R_s(\Omega)$	3.3246	1.911	1.0529
$R_d(\Omega)$	9.7042	7.1467	3.5997
C_{gs} (fF)	202.1408	244.7098	487.3104
C_{gd} (fF)	60.3007	111.829	216.8384
C_{ds} (fF)	9.58	12.07	12.4565
$R_i(\Omega)$	1.1601	0.77054	0.77246
$R_{gd}(\Omega)$	14.8492	7.2499	5.7265
G_m (mS)	0	0	0
G_{ds} (mS)	0	0	0
τ (ps)	0	0	0
Error	0.0829	0.05787	0.060343

(execution time) to complete the scanning process. Then, to avoid this assumption we developed optimization-based hybrid extraction methodologies. Finally, a detailed evaluation of MPA-, POA- and TSA-based hybrid extraction methodologies on various metrics is demonstrated in Table 5. From this table, we can easily extract out that MPA, POA and TSA techniques have the same hyperparameters and run for the same number of iterations (MNOI = 50). Furthermore, we can also notice that TSA took the least execution time for 50 iterations whereas MPA and POA took almost similar

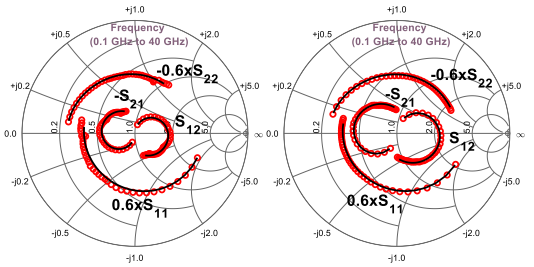

FIGURE 29. Simulated (lines) and measured (symbols) S-parameters at (left) V_{GS} = –4 V and V_{DS} = 0 V; (right) V_{GS} = –3 V and V_{DS} = 0 V (using the POA-based hybrid approach).

TABLE 8. Obtained values of the SSECM parameters using the POA-based hybrid model parameter extraction methodology.

Model Elements	GaN-on-Dia 2 x 100 μm	GaN-on-Dia 2 x 125 μm	GaN-on-Dia 4 x 125 μm
C_{pga} (fF)	2.1851	3.2231	6.0814
C_{pda} (fF)	0.7692	1.8949	1.9095
C_{pgi} (fF)	2.0854	2.4889	4.8667
C_{pdi} (fF)	52.615	99.7209	174.68
L_g (pH)	60.1023	61.5213	64.3591
L_s (pH)	0.4323	0.4615	0.6749
L_d (pH)	39.2194	40.5632	43.3738
$R_g(\Omega)$	2.4527	2.5875	1.3805
$R_s(\Omega)$	3.3246	1.9165	1.0529
$R_d(\Omega)$	9.7042	7.1147	3.5997
C_{gs} (fF)	202.1408	244.1417	487.3104
C_{gd} (fF)	60.3007	111.8465	216.8384
C_{ds} (fF)	9.58	12.11	12.4565
$R_i(\Omega)$	1.1601	0.7324	0.77246
$R_{gd}(\Omega)$	14.8492	7.0464	5.7265
G_m (mS)	0	0	0
G_{ds} (mS)	0	0	0
τ (ps)	0	0	0
Error	0.0829	0.05784	0.060343

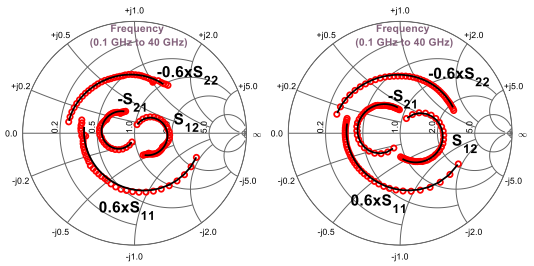

FIGURE 30. Simulated (lines) and measured (symbols) S-parameters at (left) V_{GS} = –4 V and V_{DS} = 0 V; (right) V_{GS} = –3 V and V_{DS} = 0 V (using the TSA-based hybrid approach).

execution time. The MATLAB implementation of all the OAs are simple and they produce equal accuracy at Cold-FET pinch-off condition. Furthermore, their convergence behavior is depicted through Fig. 26. In addition, based on the results, we can easily notice that both scanning-based systematic and OA-based hybrid modelling approaches accurately depict the behavior of the DUT at various operating conditions and

TABLE 9. Obtained values of the SSECM parameters using the TSA-based hybrid model parameter extraction methodology.

Model Elements	GaN-on-Dia 2 x 100 μm	GaN-on-Dia 2 x 125 μm	GaN-on-Dia 4 x 125 μm
C_{pga} (fF)	2.1851	3.2232	6.0815
C_{pda} (fF)	0.7689	1.8954	1.8849
C_{pgi} (fF)	2.0855	2.4889	4.8667
C_{pdi} (fF)	52.623	99.69	174.68
L_g (pH)	60.1025	61.5212	64.3592
L_s (pH)	0.4326	0.4618	0.67479
L_d (pH)	39.2198	40.5638	43.3749
$R_g(\Omega)$	2.4527	2.5922	1.3804
$R_s(\Omega)$	3.3246	1.9062	1.0529
$R_d(\Omega)$	9.7042	7.1165	3.5998
C_{gs} (fF)	202.1407	244.1505	487.3118
C_{gd} (fF)	60.3009	111.847	216.8364
C_{ds} (fF)	9.5796	12.12	12.4945
$R_i(\Omega)$	1.1602	0.73335	0.77246
$R_{gd}(\Omega)$	14.8499	7.0471	5.7269
G_m (mS)	0	0	0
G_{ds} (mS)	0	0	0
τ (ps)	0	0	0
Error	0.0829	0.05783	0.060343

OA-based approaches give similar error values at the testing conditions.

To extend the experimental validation of the above mentioned modelling schemes, the proposed extraction procedures are also validated on GaN-on-Diamond HEMTs of geometries 2 × 100 μm and 2 × 125 μm. The obtained values of the SSECM parameters for both the devices at cold-pinch-off conditions ((V_{GS} = –4 V, V_{DS} = 0 V) and (V_{GS} = –3 V, V_{DS} = 0 V) for 2 × 100 μm and 2 × 125 μm, respectively), are given in Tables 6-9. Furthermore, the simulation plots at the same cold-pinch-off conditions are also depicted through Figs. 27- 30. As expected both scanning-based systematic and OA-based hybrid modelling approaches have been able to accurately depict the behavior for whole frequency range. From the tabulated results (see Tables 6-9), we can notice that the pad capacitances (C_{pga} and C_{pda}) have comparable values, which reflects symmetrical pad contacts of the devices coplanar structure. The inter-electrode capacitances (C_{pgi} and C_{pdi}) are proportional to the gate-width especially the number of fingers. Similarly, it can also be observed that the intrinsic capacitances are directly related to the total gate-width, as expected. Likewise, the developed models have also been able to reproduce the effects of change in device configurations (such as total gate-width, number of fingers etc.) as reflected thorough the values of the parasitic inductances (Lg, Ls and Ld) and resistances (Rg, Rs and Rd).

At last, based on the results and above discussion, we can make the following inferences:

- The scanning-based systematic model parameter extraction methodology is easy to build, produces almost similar accuracy as optimization-based hybrid extraction and renders excellent trade-off between accuracy and execution time. However, some assumptions are needed to develop the SSECM using this approach,

which limit its physical relevance, reliability of the model parameters and generalization over the various transistor technologies

- MPA-, POA- and TSA-based hybrid model parameter extraction methodologies produce very accurate and reliable SSECMs and the obtained model parameters' values are in perfect consonance with the device structure. The proposed OA-based hybrid modelling approaches have provided almost similar values of SSECM parameters and corresponding errors. MATLAB implementation of all optimization techniques is easy. However, in terms of the execution time, TSA is the fastest among all. MPA- and POA-based hybrid extraction approaches have almost similar performance in terms of execution time, accuracy and easiness to build the models. Moreover, as OAs-based approaches in this paper do not require assumptions, they can be applied on various microwave transistor technologies

VI. CONCLUSION

A scanning-based systematic and OA-based hybrid modelling approaches, those accurately and efficiently model the small-signal behavior of GaN-on-Diamond HEMT are developed. Newly reported MPA, POA and TSA optimization techniques are employed to develop the hybrid models. We have successfully verified that the scanning-based systematic approach is able to emulate the behavior of the DUT for the whole frequency range with less execution time but requires certain assumptions, which restricts its reliability and broader applicability. Conversely, OA-based hybrid approaches produce very accurate, general and more physically relevant SSECMs but at the cost of increased execution time and efforts. Moreover, we also identified that the accuracy, complexity and number of tunable parameters of MPA, POA and TSA empowered hybrid approaches are very similar. However, MPA and POA require more execution time than TSA.

REFERENCES

[1] W. Hu and Y.-X. Guo, "An evolutionary multilayer perceptron-based large-signal model of GaN HEMTs including self-heating and trapping effects," *IEEE Trans. Microw. Theory Techn.*, vol. 70, no. 2, pp. 1146–1156, Feb. 2022.

[2] P. M. Tomé, F. M. Barradas, L. C. Nunes, J. L. Gomes, T. R. Cunha, and J. C. Pedro, "Characterization, modeling, and compensation of the dynamic self-biasing behavior of GaN HEMT-based power amplifiers," *IEEE Trans. Microw. Theory Techn.*, vol. 69, no. 1, pp. 529–540, Jan. 2021.

[3] G. Lv, W. Chen, X. Liu, F. M. Ghannouchi, and Z. Feng, "A fully integrated C-band GaN MMIC Doherty power amplifier with high efficiency and compact size for 5G application," *IEEE Access*, vol. 7, pp. 71665–71674, 2019.

[4] Y. Xu, C. Wang, H. Sun, Z. Wen, Y. Wu, R. Xu, X. Yu, C. Ren, Z. Wang, B. Zhang, T. Chen, and T. Gao, "A scalable large-signal multiharmonic model of AlGaN/GaN HEMTs and its application in C-band high power amplifier MMIC," *IEEE Trans. Microw. Theory Techn.*, vol. 65, no. 8, pp. 2836–2846, Aug. 2017.

[5] F. Zeng, J. An, G. Zhou, W. Li, H. Wang, T. Duan, L. Jiang, and H. Yu, "A comprehensive review of recent progress on GaN high electron mobility transistors: Devices, fabrication and reliability," *Electronics*, vol. 7, no. 12, p. 377, Dec. 2018.

[6] G. P. Gibiino, A. Santarelli, and F. Filicori, "A GaN HEMT global large-signal model including charge trapping for multibias operation," *IEEE Trans. Microw. Theory Techn.*, vol. 66, no. 11, pp. 4684–4697, Nov. 2018.

[7] Y. Jia, Y. Xu, Z. Wen, Y. Wu, and Y. Guo, "Analytical gate capacitance models for large-signal compact model of AlGaN/GaN HEMTs," *IEEE Trans. Electron Devices*, vol. 66, no. 1, pp. 357–363, Jan. 2019.

[8] F. Y. Huang, X. S. Tang, Z. N. Wei, L. H. Zhang, and N. Jiang, "An improved small-signal equivalent circuit for GaN high-electron mobility transistors," *IEEE Electron Device Lett.*, vol. 37, no. 11, pp. 1399–1402, Nov. 2016.

[9] A. Jarndal, S. Husain, M. Hashmi, and F. M. Ghannouchi, "Large-signal modeling of GaN HEMTs using hybrid GA-ANN, PSO-SVR, and GPR-based approaches," *IEEE J. Electron Devices Soc.*, vol. 9, pp. 195–208, 2021.

[10] G. Crupi, D. M. M.-P. Schreurs, A. Caddemi, A. Raffo, F. Vanaverbeke, G. Avolio, G. Vannini, and W. D. Raedt, "High-frequency extraction of the extrinsic capacitances for GaN HEMT technology," *IEEE Microw. Wireless Compon. Lett.*, vol. 21, no. 8, pp. 445–447, Aug. 2011.

[11] A. Jarndal, A. Hussein, G. Crupi, and A. Caddemi, "Reliable noise modeling of GaN HEMTs for designing low-noise amplifiers," *Int. J. Numer. Model., Electron. Netw., Devices Fields*, vol. 33, no. 3, May 2020, Art. no. e2585.

[12] Q. Wu, Y. Xu, J. Zhou, Y. Kong, T. Chen, Y. Wang, F. Lin, Y. Fu, Y. Jia, X. Zhao, B. Yan, and R. Xu, "Performance comparison of GaN HEMTs on diamond and SiC substrates based on surface potential model," *ECS J. Solid State Sci. Technol.*, vol. 6, no. 12, pp. Q171–Q178, 2017.

[13] Y. Chen, Y. Xu, J. Zhou, Y. Kong, T. Chen, Y. Zhang, B. Yan, and R. Xu, "Temperature-dependent small signal performance of GaN-on-diamond HEMTs," *Int. J. Numer. Modelling, Electron. Netw., Devices Fields*, vol. 33, no. 3, May 2020, Art. no. e2620.

[14] H. Luo, X. Yan, J. Zhang, and Y. Guo, "A neural network-based hybrid physical model for GaN HEMTs," *IEEE Trans. Microw. Theory Techn.*, vol. 70, no. 11, pp. 4816–4826, Nov. 2022.

[15] S. Khandelwal, Y. S. Chauhan, and T. A. Fjeldly, "Analytical modeling of surface-potential and intrinsic charges in AlGaN/GaN HEMT devices," *IEEE Trans. Electron Devices*, vol. 59, no. 10, pp. 2856–2860, Oct. 2012.

[16] H. Qi, J. Benedikt, and P. J. Tasker, "Nonlinear data utilization: From direct data lookup to behavioral modeling," *IEEE Trans. Microw. Theory Techn.*, vol. 57, no. 6, pp. 1425–1432, Jun. 2009.

[17] A. Jarndal, S. Husain, and M. Hashmi, "Genetic algorithm initialized artificial neural network based temperature dependent small-signal modeling technique for GaN high electron mobility transistors," *Int. J. RF Microw. Comput.-Aided Eng.*, vol. 31, no. 3, Mar. 2021, Art. no. e22542.

[18] Z. Marinković, G. Crupi, A. Caddemi, V. Marković, and D. M. M. Schreurs, "A review on the artificial neural network applications for small-signal modeling of microwave FETs," *Int. J. Numer. Model., Electron. Netw., Devices Fields*, vol. 33, no. 3, May 2020, Art. no. e2668.

[19] S. Husain, M. Hashmi, and F. M. Ghannouchi, "Comprehensive investigation and comparative analysis of machine learning-based small-signal modelling techniques for GaN HEMTs," *IEEE J. Electron Devices Soc.*, vol. 10, pp. 1015–1032, 2022.

[20] A. Jarndal, S. Husain, and M. Hashmi, "On temperature-dependent small-signal modelling of GaN HEMTs using artificial neural networks and support vector regression," *IET Microw., Antennas Propag.*, vol. 15, no. 8, pp. 937–953, Jul. 2021.

[21] A. Khusro, S. Husain, M. S. Hashmi, A. Q. Ansari, and S. Arzykulov, "A generic and efficient globalized kernel mapping-based small-signal behavioral modeling for GaN HEMT," *IEEE Access*, vol. 8, pp. 195046–195061, 2020.

[22] A. Khusro, S. Husain, M. S. Hashmi, and A. Q. Ansari, "Small signal behavioral modeling technique of GaN high electron mobility transistor using artificial neural network: An accurate, fast, and reliable approach," *Int. J. RF Microw. Comput.-Aided Eng.*, vol. 30, no. 4, Apr. 2020, Art. no. e22112.

[23] A. Khusro, M. S. Hashmi, and A. Q. Ansari, "Enabling the development of accurate intrinsic parameter extraction model for GaN HEMT using support vector regression (SVR)," *IET Microw., Antennas Propag.*, vol. 13, no. 9, pp. 1457–1466, Jul. 2019.

[24] R. G. Brady, C. H. Oxley, and T. J. Brazil, "An improved small-signal parameter-extraction algorithm for GaN HEMT devices," *IEEE Trans. Microw. Theory Techn.*, vol. 56, no. 7, pp. 1535–1544, Jul. 2008.

[25] Y. Chen, Y. Xu, Y. Luo, C. Wang, Z. Wen, B. Yan, and R. Xu, "A reliable and efficient small-signal parameter extraction method for GaN HEMTs," *Int. J. Numer. Modelling, Electron. Netw., Devices Fields*, vol. 33, no. 3, May 2020, Art. no. e2540.

[26] L. Zhai, H. Cai, S. Wang, J. Zhang, and S. Yang, "A reliable parameter extraction method for the augmented GaN high electron mobility transistor small-signal model," *Int. J. RF Microw. Comput.-Aided Eng.*, vol. 32, no. 8, Aug. 2022, Art. no. e23210.
[27] Z. Wen, Y. Xu, C. Wang, X. Zhao, and R. Xu, "An efficient parameter extraction method for GaN HEMT small-signal equivalent circuit model," *Int. J. Numer. Modelling, Electron. Netw., Devices Fields*, vol. 30, no. 1, Jan. 2017, Art. no. e2127.
[28] G. Crupi, D. Xiao, D. M. M.-P. Schreurs, E. Limiti, A. Caddemi, W. De Raedt, and M. Germain, "Accurate multibias equivalent-circuit extraction for GaN HEMTs," *IEEE Trans. Microw. Theory Techn.*, vol. 54, no. 10, pp. 3616–3622, Oct. 2006.
[29] Y. Liu, F. Cao, X. Xiong, J. Huang, and W. Deng, "Parameter extraction for small-signal model of GaN HEMTs on SiC substrates based on modified firefly algorithm," *Int. J. RF Microw. Comput.-Aided Eng.*, vol. 32, no. 12, Dec. 2022, Art. no. e23518.
[30] A. Majumder, S. Chatterjee, S. Chatterjee, S. S. Chaudhari, and D. R. Poddar, "Optimization of small-signal model of GaN HEMT by using evolutionary algorithms," *IEEE Microw. Wireless Compon. Lett.*, vol. 27, no. 4, pp. 362–364, Apr. 2017.
[31] M. Al Sabbagh, M. C. E. Yagoub, and J. Park, "New small-signal extraction method applied to GaN HEMTs on different substrates," *Int. J. RF Microw. Comput.-Aided Eng.*, vol. 30, no. 9, Sep. 2020, Art. no. e22291.
[32] S. Colangeli, W. Ciccognani, R. Cleriti, M. Palomba, and E. Limiti, "Optimization-based approach for scalable small-signal and noise model extraction of GaN-on-SiC HEMTs," *Int. J. Numer. Model., Electron. Netw., Devices Fields*, vol. 30, no. 1, Jan. 2017, Art. no. e2135.
[33] A. Majumder, S. Chatterjee, S. Bose, S. Chatterjee, S. S. Chaudhari, and D. R. Poddar, "Differential evolution based small signal modeling of GaN HEMT," *Int. J. RF Microw. Comput.-Aided Eng.*, vol. 29, no. 6, Jun. 2019, Art. no. e21693.
[34] A. S. Hussein and A. H. Jarndal, "Reliable hybrid small-signal modeling of GaN HEMTs based on particle-swarm-optimization," *IEEE Trans. Comput.-Aided Design Integr. Circuits Syst.*, vol. 37, no. 9, pp. 1816–1824, Sep. 2018.
[35] A. Jarndal, X. Du, and Y. Xu, "Modelling of GaN high electron mobility transistor on diamond substrate," *IET Microw., Antennas Propag.*, vol. 15, no. 6, pp. 661–673, May 2021.
[36] C. Roff, J. Benedikt, P. J. Tasker, D. J. Wallis, K. P. Hilton, J. O. Maclean, D. G. Hayes, M. J. Uren, and T. Martin, "Analysis of DC–RF dispersion in AlGaN/GaN HFETs using RF waveform engineering," *IEEE Trans. Electron Devices*, vol. 56, no. 1, pp. 13–19, Jan. 2009.
[37] G. Crupi, "An extensive experimental analysis of the kink effects in S_{22} and h_{21} for a GaN HEMT," *IEEE Trans. Microw. Theory Techn.*, vol. 62, no. 3, pp. 513–520, Mar. 2014.
[38] A. Faramarzi, M. Heidarinejad, S. Mirjalili, and A. H. Gandomi, "Marine predators algorithm: A nature-inspired metaheuristic," *Expert Syst. Appl.*, vol. 152, Aug. 2020, Art. no. 113377.
[39] P. Trojovský and M. Dehghani, "Pelican optimization algorithm: A novel nature-inspired algorithm for engineering applications," *Sensors*, vol. 22, no. 3, p. 855, Jan. 2022.
[40] S. Kaur, L. K. Awasthi, A. L. Sangal, and G. Dhiman, "Tunicate swarm algorithm: A new bio-inspired based metaheuristic paradigm for global optimization," *Eng. Appl. Artif. Intell.*, vol. 90, Apr. 2020, Art. no. 103541.

SADDAM HUSAIN received the B.Tech. degree from the Galgotias College of Engineering and Technology, Noida, India, in 2016, and the M.Tech. degree from Jamia Millia Islamia (A Central University), New Delhi, India, in 2019. He is currently pursuing the Ph.D. degree in electrical engineering from Nazarbayev University, Astana, Kazakhstan. He held research positions with the High Speed Electronics Laboratory, IIIT Delhi, India, and the Research Institute of Sciences and Engineering (RISE), University of Sharjah, United Arab Emirates. His research interests include machine learning-based modeling and optimization, measurement, characterization, and modeling of RF/Microwave devices, and power amplifier design.

ANWAR JARNDAL (Senior Member, IEEE) received the Ph.D. degree in electrical engineering from the University of Kassel, Kassel, Germany, in 2006. He was a Postdoctoral Fellow with École de Technologie Supérieure (ETS), Quebec University, Canada. He is currently a Full Professor with the Department of Electrical Engineering, University of Sharjah. He has published more than 140 internationally peer-reviewed publications. His research interests include active device modeling, measurements and characterization techniques, power amplifier design, low-noise amplifier design, active sensors, local and global optimizations, artificial neural networks, machine learning, fuzzy logic, radio channel modeling, and wireless power transfer. He is serving as a reviewer for more than 25 international journals. He received the Annual Incentives Award for the Distinguished Faculty in Scientific Research from the University of Sharjah. He was also classified as one of the World's Top 2% Scientists 2020 (Stanford University).

MOHAMMAD HASHMI (Senior Member, IEEE) received the M.S. degree from the Darmstadt University of Technology, Darmstadt, Germany, and the Ph.D. degree from Cardiff University, Cardiff, U.K. He held research and engineering positions with the University of Calgary, Canada; Cardiff University, U.K.; Thales Electronics GmbH, Germany; and the Philips Technology Center, Germany. He is currently an Associate Professor with the School of Engineering and Digital Sciences, Nazarbayev University, Kazakhstan. He has authored or coauthored one book and more than 250 publications and holds three patents (one pending). His current research interests include advanced RF technology, broadband linear and efficient power amplifiers for mobile and satellite applications, high- and low-frequency instrumentation, and hardware security and trust. He serves as an Associate Editor for IEEE *Microwave Magazine*.

FADHEL M. GHANNOUCHI (Fellow, IEEE) is currently a Professor, the Alberta Innovates/Canada Research Chair, and the Director of the iRadio Laboratory with the Department of Electrical and Computer Engineering, University of Calgary, Alberta, Canada, and a part-time Thousand Talent Professor with the Department of Electronics Engineering, Tsinghua University, Beijing, China. He is also the Co-Founder of three University spun-off companies. He has published more than 800 refereed papers, and six books, and holds 25 patents (three pending). His research interests include RF and wireless communications, nonlinear modeling of microwave devices and communications systems, design of power- and spectrum-efficient microwave amplification systems, and design of SDR systems for wireless, and optical and satellite communications applications.

He is a fellow of the Academy of Science of the Royal Society of Canada, the Canadian Academy of Engineering, and the Engineering Institute of Canada, the Institution of Engineering and Technology (IET).